coatings

MDPI

Article

Synergistic Disinfection of Photocatalytic Nanomaterials Exposed to UVC, Electricity and Magnetic Fields Against *Candida albicans*

María Cristina Grijalva-Castillo [1], Renee Joselin Saénz-Hernández [1], Adrián Alberto Cobos-Márquez [1], Francisco Alonso Herrera-Ojeda [2], Fernando Efraín Díaz-Chávez [2], Irving Ricardo Acosta-Galindo [2], César Leyva-Porras [1], Alva Rocío Castillo-González [2], María Alejandra Favila-Pérez [2], Celia María Quiñonez-Flores [2], Javier Camarillo Cisneros [2] and Carlos Arzate-Quintana [2,*]

[1] Secihti-Centro de Investigación en Materiales Avanzados (CIMAV), Chihuahua 31135, Mexico; cristina.grijalva@cimav.edu.mx (M.C.G.-C.); joselin.saenz@cimav.edu.mx (R.J.S.-H.); adrian.cobos@cimav.edu.mx (A.A.C.-M.); cesar.leyva@cimav.edu.mx (C.L.-P.)
[2] Facultad de Medicina y Ciencias Biomédicas, Universidad Autónoma de Chihuahua, Chihuahua 31125, Mexico; a342996@uach.mx (F.A.H.-O.); a342959@uach.mx (F.E.D.-C.); a346482@uach.mx (I.R.A.-G.); acastillo@uach.mx (A.R.C.-G.); afavila@uach.mx (M.A.F.-P.); cquinonezf@uach.mx (C.M.Q.-F.); javier.camarillo@uach.mx (J.C.C.)
* Correspondence: carzate@uach.mx

Abstract

Nosocomial infections caused by *Candida albicans* pose serious challenges to healthcare systems due to their persistence on medical surfaces and resistance to conventional disinfectants. This study evaluates antifungal properties of SnO_2 doped with silver and cuprite nanoparticles and WO_3 thin films, as well as cobalt ($CoFe_2O_4$) and cobalt–nickel ($Co_{0.5}Ni_{0.5}Fe_2O_4$) ferrite nanoparticles, activated by ultraviolet C (UVC) radiation, direct electric current (up to 100 V), and magnetic fields. SnO_2 films were synthesized by Spray Pyrolysis and WO_3 by Sputtering deposition, Ferrites nanoparticles by sol–gel, while metallic nanoparticles were synthetized via chemical reduction. Characterization consisted mainly of SEM, TEM, and XRD, and their antimicrobial activity was tested against *C. albicans*. WO_3 films achieved 86.2% fungal inhibition after 5 min of UVC exposure. SnO_2 films doped with nanoparticles reached 100% inhibition when combined with UVC and 100 V. Ferrite nanoparticles alone showed moderate activity (21.9%–40.4%) but exhibited strong surface adhesion to fungal cells, indicating potential for magnetically guided antifungal therapies. These results demonstrate the feasibility of using multifunctional nanomaterials for rapid, non-chemical disinfection. The materials are low-cost, scalable, and adaptable to hospital settings, making them promising candidates for reducing healthcare-associated fungal infections through advanced surface sterilization technologies.

Keywords: antimicrobial photocatalysis; tin oxide; cobalt ferrites; tungsten oxide; silver nanoparticles; cuprite nanoparticles

check for updates

Academic Editors: Simona Liliana Iconaru and Min Zhang

Received: 28 June 2025
Revised: 12 August 2025
Accepted: 13 August 2025
Published: 19 August 2025

Citation: Grijalva-Castillo, M.C.; Saénz-Hernández, R.J.; Cobos-Márquez, A.A.; Herrera-Ojeda, F.A.; Díaz-Chávez, F.E.; Acosta-Galindo, I.R.; Leyva-Porras, C.; Castillo-González, A.R.; Favila-Pérez, M.A.; Quiñonez-Flores, C.M.; et al. Synergistic Disinfection of Photocatalytic Nanomaterials Exposed to UVC, Electricity and Magnetic Fields Against *Candida albicans*. *Coatings* **2025**, *15*, 968. https://doi.org/10.3390/coatings15080968

Copyright: © 2025 by the authors. Licensee MDPI, Basel, Switzerland. This article is an open access article distributed under the terms and conditions of the Creative Commons Attribution (CC BY) license (https://creativecommons.org/licenses/by/4.0/).

1. Introduction

Candida albicans is the most common fungal pathogen associated with hospital-acquired infections and is a leading cause of morbidity and mortality in immunocompromised patients. Its prevalence in healthcare settings has been linked to extended hospital stays, increased treatment costs, and mortality rates that can reach up to 70% in high-risk populations such as neonates and immunosuppressed individuals [1–3]. In the United

States alone, the management of candidiasis has been estimated to cost approximately USD 1.4 billion annually [4].

The increasing incidence of drug-resistant *C. albicans* strains complicates effective treatment and highlights the urgent need for improved infection control strategies [5–7]. Given the high cost and complexity of developing new antifungal agents, preventive measures—particularly surface disinfection technologies—are gaining attention. Antimicrobial coatings on hospital surfaces, including medical instruments, walls, and furnishings, can help reduce fungal colonization and improve disinfection protocols [6,8].

Photocatalytic materials have demonstrated antifungal activity through the generation of reactive oxygen species (ROS), especially under ultraviolet C (UVC) light [9,10]. Incorporating metal or metal oxide nanoparticles into semiconductors, such as silver or cuprite, can enhance photocatalytic efficiency by promoting charge separation and increasing ROS production [10]. Among these materials, tin oxide (SnO_2) and tungsten oxide (WO_3) have shown promising photocatalytic and antimicrobial properties, particularly under UVC illumination [10,11]. Notably, SnO_2 exhibits higher electrical conductivity than many other photocatalysts, such as TiO_2 or ZnO, which facilitates more efficient charge transport and reduces electron–hole recombination [12]. A key reason for SnO_2's good electrical conductivity is its electronic structure. Research shows that SnO_2 is a better electron acceptor than other photocatalytic materials because its conduction band is more favorably positioned, which helps separate charges and improve electron movement. This is also supported by its lower conduction band potential, making it effective in systems that need efficient charge transfer. Although SnO_2 has a wider band gap than some other materials, it still shows excellent conductivity—mainly due to its structure and the presence of defects that allow charge carriers to move more easily. These properties make SnO_2 particularly suitable for activation under electric fields, enhancing its antimicrobial performance. Additionally, it can be incorporated into other photocatalytic materials to improve their electrical conductivity [13–15]. On the other hand, while WO_3 has demonstrated good photocatalytic behavior and chemical stability, its antimicrobial applications have been explored in fewer studies, making it a less conventional but potentially valuable alternative. Both materials are low-cost, chemically stable, and compatible with scalable thin-film fabrication, positioning them as strong candidates for use in hospital surface disinfection technologies.

Although this study did not include ZnO and TiO_2, it is important to note that both are widely recognized for their outstanding photocatalytic properties. In particular, TiO_2 is considered one of the most effective and extensively studied photocatalysts, owing to its high photostability, non-toxicity, and strong oxidative capacity under UV irradiation [12]. However, these materials were not selected for the present work because their low electrical conductivity makes them less suitable for applications involving electrical current-assisted disinfection. Despite this limitation, their excellent performance under light exposure alone makes them promising candidates. Future studies will explore the photocatalytic activity of TiO_2 and ZnO, both independently and in combination with other enhancement strategies, to better understand their potential under light-only conditions.

In addition, cobalt ferrite ($CoFe_2O_4$) and cobalt–nickel ferrite ($Co_{0.8}Ni_{0.2}Fe_2O_4$) nanoparticles exhibit magnetic responsiveness and surface adhesion to microbial cells, enabling their use in magnetically targeted antimicrobial strategies [16]. These ferrites also possess semiconducting properties, making them suitable for integration with photocatalytic systems. The combination of photocatalysts and ferrites may lead to synergistic effects when activated by UVC light, electric current, or magnetic fields.

This study investigates the antimicrobial performance of SnO_2 doped with silver (AgNP) and cuprite (Cu_2O) nanoparticles, WO_3 thin films, and ferrite nanoparticles under different physical activation conditions. These conditions (such as UVC irradiation,

electric fields, and magnetic fields) are unlikely to induce microbial resistance and do not require the use of potentially toxic chemical disinfectants. By integrating photocatalytic and magneto-responsive mechanisms, this work aims to develop a multifunctional surface treatment capable of effectively inactivating *C. albicans*. The proposed approach contributes to infection control strategies in hospital environments by offering a fast, easy-to-apply, and low-risk alternative for disinfection that minimizes exposure hazards for healthcare personnel.

2. Materials and Methods

2.1. Cuprite and Silver Nanoparticles Synthesis and Analysis

Silver nanoparticle (AgNP) synthesis was carried out via chemical reduction by adding a 0.01 M sodium borohydride ($NaBH_4$) solution dropwise (one drop per second) to a 0.005 M silver nitrate ($AgNO_3$) solution. The reduction reaction continued until the solution turned dark gray, indicating nanoparticle formation.

Copper (I) oxide nanoparticles (Cu_2O NP) were synthesized by dropwise addition (one drop per second) of a 0.1 M $NaBH_4$ solution to a reaction mixture containing 0.1 M copper (II) sulfate pentahydrate ($CuSO_4 \cdot 5H_2O$), 0.02 M gallic acid, and 4% v/v Triton X-100. The mixture was maintained at 80 °C, and the synthesis proceeded until the color changed to light brown, indicating the formation of Cu_2O nanoparticles.

Both types of nanoparticles were characterized by scanning electron microscopy (SEM) (JEOL, Tokyo, Japan) to evaluate morphology, and their elemental composition was analyzed using energy-dispersive X-ray spectroscopy (EDS) (Akishima, Tokyo, Japan). Additionally, nanoparticle morphology and crystalline structure were confirmed by X-ray diffraction (XRD) (Bruker, Karlsruhe, Germany).

2.2. SnO_2 Films Synthesis and Characterization

Tin oxide (SnO_2) thin films were synthesized using the spray pyrolysis technique [5,17]. This process involved atomizing a 0.5 M solution of stannous chloride ($SnCl_2$) through a nebulizer and directing the aerosol onto glass substrates heated to 400–450 °C. Doping with nanoparticles was achieved by depositing 10 µL of the nanoparticle suspension onto a 1 cm^2 area of the SnO_2 films, followed by drying at room temperature.

The surface topography and film thickness were examined using scanning electron microscopy (SEM), while elemental composition was analyzed via energy-dispersive X-ray spectroscopy (EDS). Crystalline structure and phase composition of the films were assessed by X-ray diffraction (XRD).

2.3. Ferrite Nanoparticle Synthesis and Characterization

Cobalt ferrite ($CoFe_2O_4$) and cobalt–nickel ferrite ($Co_{0.8}Ni_{0.2}Fe_2O_4$) nanoparticles were synthesized using the sol–gel method. Stoichiometric amounts of high-purity (>99%) commercial powders of cobalt nitrate ($Co(NO_3)_2 \cdot 6H_2O$), iron nitrate ($Fe(NO_3)_3 \cdot 9H_2O$), and nickel nitrate ($Ni(NO_3)_2 \cdot 6H_2O$) were dissolved in ethylene glycol ($C_2H_6O_2$) at a ratio of 12 mL per 0.005 moles of ferrite. The solution was stirred at 80 °C for 2 h until a viscous gel formed. The resulting gel was dried in an oven at 100 °C for 24 h to remove residual liquids. Finally, the obtained powder was calcined at 500 °C for 4 h with a heating rate of 10 °C/min.

The morphology and elemental composition of the synthesized nanoparticles were analyzed using a Hitachi Model 7700 transmission electron microscope (TEM) (Hitachinaka, Ibaraki, Japan). X-ray diffraction (XRD) patterns were collected using a PANalytical X'Pert PRO diffractometer equipped with an X'Celerator detector (Malvern Panalytical, Almelo, The Netherlands) in Bragg–Brentano configuration. The scans covered a 2θ range of

10° to 80° with a step size of 0.017° and an acquisition time of 14 s, using copper Kα radiation (λ = 1.5406 Å). Magnetization curves were measured at room temperature using a Quantum Design physical property measurement system (PPMS) with a vibrating sample magnetometry (VSM) probe. The maximum applied magnetic field was 20 kOe.

2.4. WO_3 Thin Films Growth by Sputtering

Thin films were deposited onto Corning 7059 glass substrates. Prior to deposition, the substrates were cleaned using ultrasonic agitation—first in isopropanol, followed by acetone—for several minutes to eliminate any surface contaminants. A 2-inch diameter metallic tungsten trioxide (WO_3) target with 99.99% purity was used as the source material. Deposition was performed using an ATC Orion 3 system (AJA International). Argon gas was introduced to generate the plasma, and before initiating the film growth, the target surface was pre-sputtered for 5 min with the shutter closed to remove residual surface impurities.

For reactive sputtering, oxygen gas was then introduced into the chamber, and the argon-to-oxygen flow ratio was adjusted to 3:1, resulting in a total pressure of 0.66 Pa. All depositions were carried out at room temperature, with the substrate positioned 28 cm from the target and rotated at 40 rpm to ensure uniform film thickness. A DC power supply set to 60 W was used for all depositions. The only variable parameter was the deposition time, which was adjusted to produce films of different thicknesses.

Following deposition, the films were characterized using X-ray diffraction (XRD), scanning electron microscopy (SEM), atomic force microscopy (AFM) (Asylum Research, Santa Barbara, CA, USA), and Raman spectroscopy (HORIBA LabRAM HR VIS-633, Kyoto, Japan). As-deposited films were found to be amorphous. Therefore, a thermal annealing process, was applied: the WO_3 films were heated in air from room temperature to 500 °C for 1 min using a heating rate of 2 °C/min and then cooled back to room temperature at the same rate in a Barnstead Thermolyne Type 47,900 furnace (Dubuque, IA, USA). After annealing, the films underwent the same characterizations along with additional analyses [18].

2.5. Viability Assays of C.albicans Exposed to Physical Treatments

Candida albicans ATCC 10231 was selected for microbiological testing due to its clinical relevance in hospital environments. The strain was maintained on Sabouraud Dextrose Agar at 4 °C. Prior to experimentation, yeast cells were activated by incubation in Sabouraud Dextrose Broth at 37 °C for 24 h to ensure metabolic activity for subsequent antimicrobial assays. The working suspension was then standardized to a concentration of 1×10^8 cells/mL using a Neubauer hemocytometer (Visionaren, Lauda-Konigshofen, Germany).

The antimicrobial activity was tested in sterile conditions inside a Purifier Biological Safety cabinet Class II, Type A2 (LABCONCO, Kansas City, MO, USA) by exposure to a variety of physical treatments: electrical current was generated by a Power supply (PowerEase, Taipei, Taiwan); UVC treatments were applied inside a UV sterilization chamber (American Medical Systems, Jalisco, México); and magnetic fields (2959 Gauss) were generated with a neodymium magnet (1.875″ X 0.875″ X 0.393″) (Magnetika Saiffe, Zapopan, México).

2.5.1. SnO_2 Antimicrobial Assays on Dry Surface

The SnO_2 antimicrobial assays were conducted using films either undoped or doped with metallic nanoparticles. Samples were subjected to three different treatment conditions: (1) exposure to 254 nm ultraviolet light for 5 min, (2) exposure to an electric field of 100 V and 1–2 mA for 5 min, and (3) simultaneous exposure to both UV light and electric field

for 5 min. A glass surface inoculated with *Candida albicans* served as the control and was considered to represent 100% cell viability.

Following treatment, all samples—including the treated films and the glass control—were placed into sterile culture tubes (15 × 100 mm) containing 10 mL of Sabouraud Dextrose Broth and incubated at 37 °C for 24 h. Colony-forming units (CFUs) were quantified using a Neubauer hemocytometer under an optical microscope at 40× magnification (Figure 1).

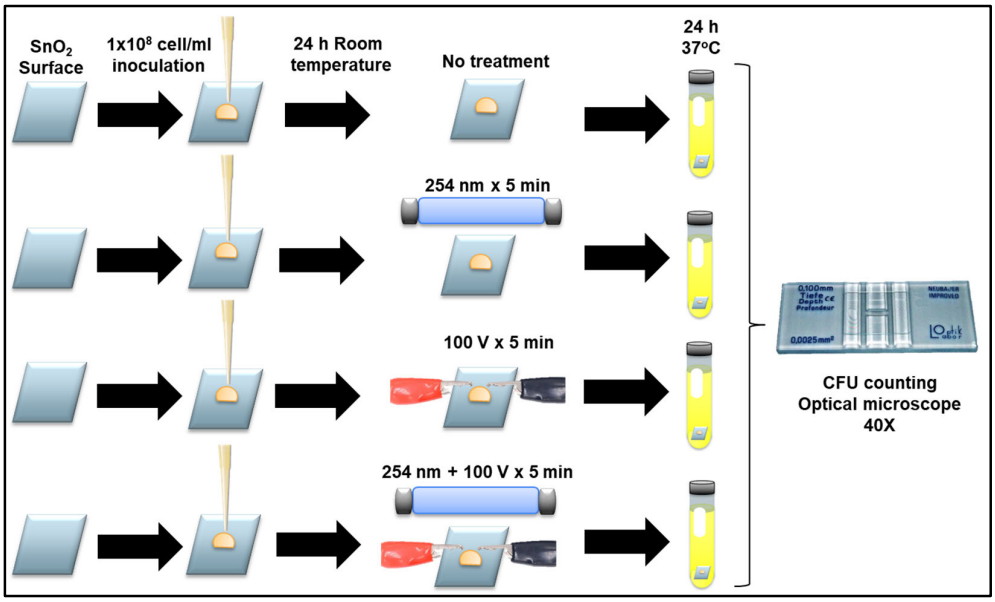


Figure 1. Schematic representation of the antimicrobial assay methodology for SnO_2 thin films exposed to UVC irradiation and electric current against the human pathogen *C.albicans*. Experiments were performed in triplicate, and the inhibition percentage was calculated relative to an inoculated glass surface used as the viability control.

2.5.2. Ferrite Nanoparticles Antimicrobial Assays in Aqueous Media

Antifungal activity of $CoFe_2O_4$ and $Co_{0.8}Ni_{0.2}Fe_2O_4$ nanoparticles was evaluated in Sabouraud Dextrose Broth using 5 cm Petri dishes. A suspension of *C. albicans* was prepared, and 10 µL of this suspension was added to 2 mL of broth per condition.

The following experimental treatments were tested, each containing 6.5 mg/mL of ferrite nanoparticles:

Treatment 1: Nanoparticles only.
Treatment 2: Nanoparticles + 5 min of UVC radiation.
Treatment 3: Nanoparticles + 5 min exposure to 100 V electric current.
Treatment 4: Nanoparticles + 5 min of UVC + 100 V electric current.
Treatment 5: Nanoparticles + 5 min of UVC, 100 V electric current, and a magnetic field.

Electric current was applied using graphite electrodes, and all treatments were performed in triplicate. After the 5 min exposure period, the viability of *C. albicans* was quantified using a Neubauer hemocytometer, and results were expressed as colony-forming units per milliliter (CFU/mL).

Two types of controls were included:

1. Positive control (untreated): Broth inoculated with *C. albicans* but without nanoparticles or physical treatments, representing 100% viability.
2. Physical treatment controls: Each physical treatment was also applied in the absence of nanoparticles to evaluate the specific contribution of the ferrite materials.

Statistical comparisons were conducted using Student's *t*-test.

2.5.3. WO_3 Antimicrobial Assays in Dry Surfaces

For the WO_3 thin films, only UVC exposure was applied, as the films exhibited no measurable electrical conductivity, making current-assisted disinfection impractical. Each film was inoculated with 10 µL of the microbial working solution and air-dried at room temperature for 24 h. An inoculated glass surface not exposed to UVC served as a control to evaluate any intrinsic chemical inhibition by WO_3. To assess the photocatalytic contribution to UVC-based disinfection, an additional inoculated glass surface was exposed to UVC radiation and used as a baseline for comparison with the WO_3-coated samples.

All samples were subjected to UVC radiation (254 nm) for 5 min, then transferred into sterile culture tubes (15 × 100 mm) containing 10 mL of Sabouraud Dextrose Broth and incubated at 37 °C for 24 h. Colony-forming units (CFUs) were quantified using a Neubauer hemocytometer (Visionären, Lauda-Königshofen, Germany) under an optical microscope at 40× magnification, following previously reported methodologies [3,5].

2.6. Scanning Electron Microscopy of C.albicans Exposed to Treatments

SEM analysis of WO_3 and SnO_2 thin film surfaces was conducted by inoculating each film with 10 µL of a distilled water suspension containing 1×10^8 *C. albicans* cells/mL. The samples were allowed to dry at room temperature for 24 h. Subsequently, the films were exposed to the physical treatments described previously and then placed in a vacuum purge desiccator (JEOL, Tokyo, Japan) until analysis. Prior to SEM imaging, all samples were sputter-coated with gold using an evaporator/sputtering system (Denton Vacuum, Moorestown, NJ, USA) under conditions of 40 mA and 300 millitorr.

For SEM analysis of *C. albicans* exposed to $CoFe_2O_4$, $Co_{0.8}Ni_{0.2}Fe_2O_4$ nanoparticles and the corresponding physical treatments (as outlined in Figure 2), yeast cells were fixed post-treatment with 10% glutaraldehyde and washed three times with phosphate-buffered saline (PBS). Residual salts were removed with distilled water, and samples were then dried at room temperature in a vacuum purge desiccator (JEOL EMDSC-U10A, Tokio, Japan). As with the film samples, these were also sputter-coated with gold prior to SEM observation.

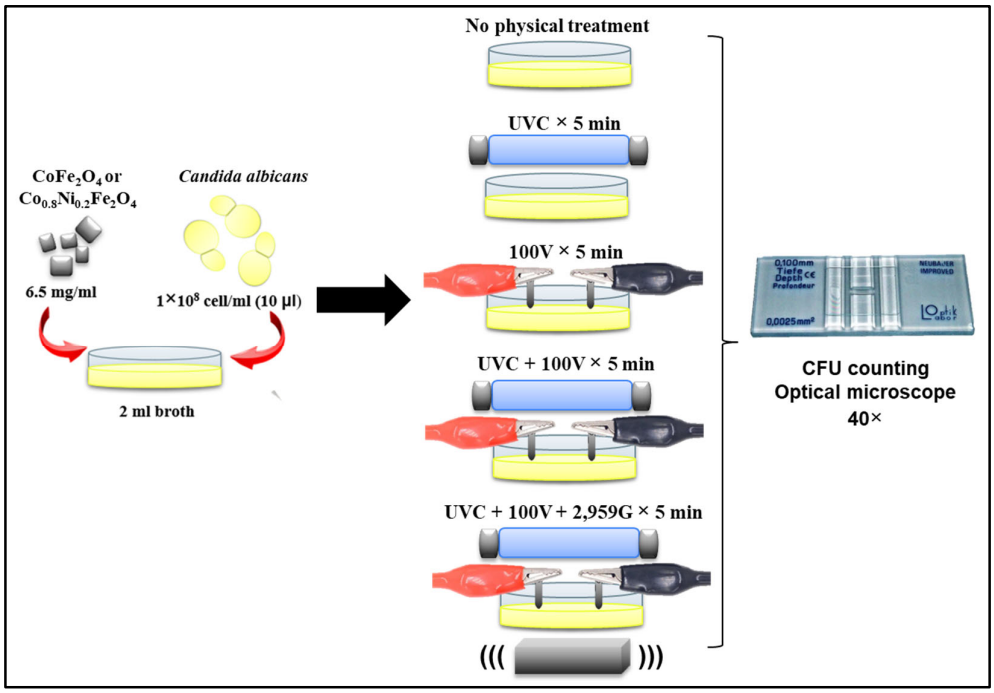


Figure 2. Schematic representation of the antimicrobial assay methodology for $CoFe_2O_4$ and $Co_{0.8}Ni_{0.2}Fe_2O_4$ nanoparticles against *Candida albicans*, under exposure to UVC irradiation, electric current, and magnetic fields.

3. Results

3.1. Cuprite and Silver Nanoparticle Characterization

EDS analysis confirmed the presence of copper and oxygen in the samples, and SEM micrographs showed cubic particles of an average size of 95.9 nm; the XRD analysis identified a cuprite phase, corresponding to cubic Cu_2O. The peaks were indexed to the Pn-3m space group, which is characteristic of the cuprite crystal structure. The measured lattice parameter of a = 4.268 Å aligns well with reported values for crystalline Cu_2O. This confirms the formation of phase-pure cuprous oxide (Cu_2O) with a well-defined cubic structure.

The composition of AgNPs was confirmed by both energy-dispersive X-ray spectroscopy (EDS) and X-ray diffraction (XRD). The XRD pattern matched the reference card 01-071-4613, corresponding to metallic silver with a cubic crystal system and Fm-3m space group. The calculated lattice parameter was a = 4.0880 Å, consistent with standard values for crystalline Ag. The average particle size, estimated from scanning electron microscopy (SEM) micrographs, was 40.3 nm. Additionally, the sharp and well-defined diffraction peaks in the XRD pattern indicate a high degree of crystallinity. No secondary phases or impurities were detected, confirming the phase purity of the synthesized nanoparticles. EDS analysis further verified the elemental composition, showing strong silver signals with minimal presence of other elements, likely originating from the substrate or residual synthesis by-products.

3.2. Characterization of SnO_2 Films

Topographical and microscopic characterization using SEM at 10,000× magnification (Figure 3A) revealed a tetragonal crystal structure. A cross-sectional image of the film (Figure 3B) showed an approximate thickness of 1 µm. Elemental composition analysis by EDS (Figure 3C) confirmed the presence of tin, oxygen, and trace elements. The X-ray diffraction analysis (Figure 3D) indicates that all samples crystallized in the tetragonal phase of SnO_2. The observed diffraction peaks correspond to the $P4_2/mnm$ space group, which is the standard space group for the rutile-type structure of tin dioxide (Cassiterite).

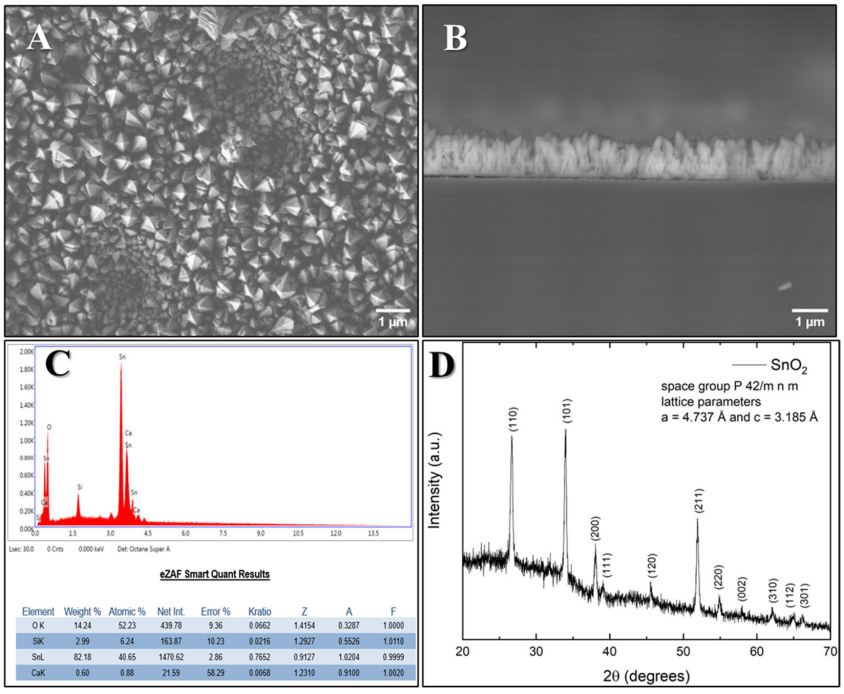


Figure 3. SEM analysis of the SnO_2 film showing: (**A**) surface topography and (**B**) cross-sectional thickness. (**C**) EDS analysis confirmed the elemental composition of the film, while XRD analysis (**D**) Identified the tetragonal cassiterite phase as the dominant crystalline structure.

The lattice parameters measured were a = 4.737 Å and c = 3.185 Å, consistent with the known values for tetragonal SnO_2. This confirms the successful synthesis of the rutile SnO_2 crystalline phase without detectable secondary phases or impurities. The precise lattice parameters indicate a well-ordered crystalline structure, which is important for the material's electronic and photocatalytic properties.

3.3. Characterization of Ferrite Nanoparticles

TEM analysis (Figure 4A) revealed that the $CoFe_2O_4$ nanoparticles possess a predominantly cubic morphology with an average particle size of 22.99 nm, as shown in the size distribution histogram (Figure 4B). X-ray diffraction (XRD) analysis (Figure 4C) confirmed that the nanoparticles adopt a spinel-type cubic ferrite structure, characteristic of cobalt ferrite ($CoFe_2O_4$). The diffraction pattern matched the standard face-centered cubic (FCC) structure with space group Fd-3m (No. 227), corresponding to ICSD reference #195530. The calculated lattice parameter was a = 8.375 Å, which is in agreement with reported values for pure cobalt ferrite. These findings confirm the formation of a well-defined, single-phase spinel structure, which is critical for anticipating the material's magnetic, electrical, and catalytic behavior.

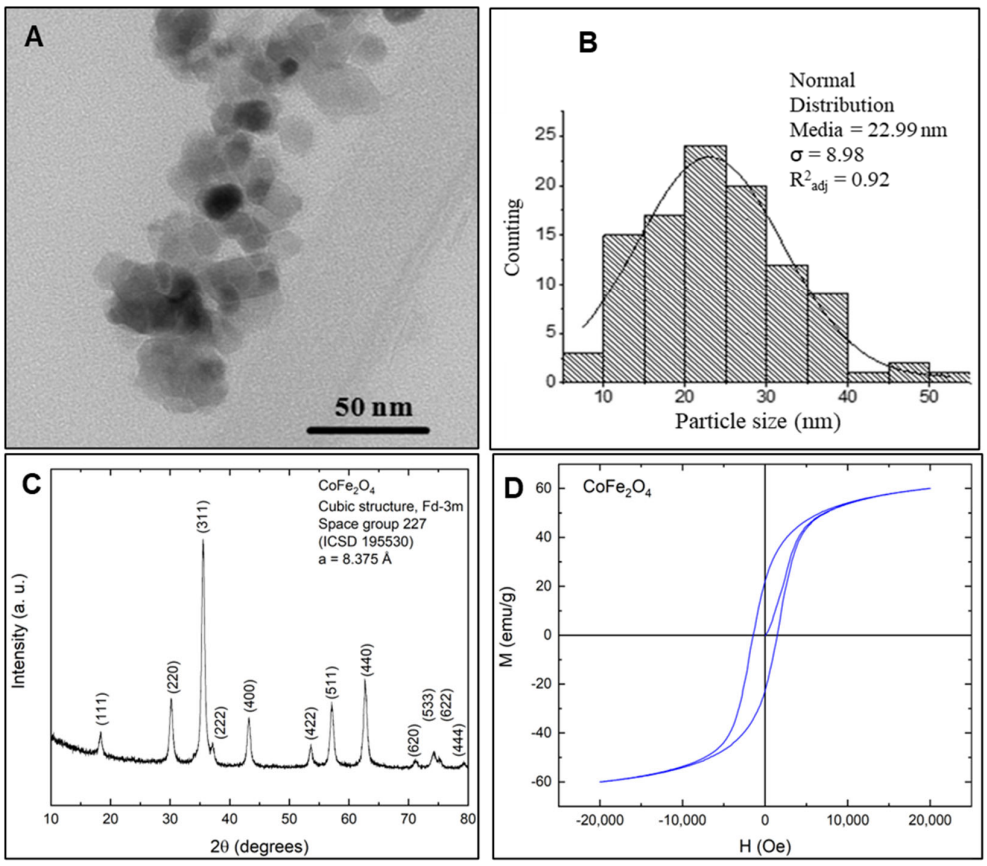


Figure 4. Characterization of $CoFe_2O_4$ nanoparticles, including: (**A**) TEM image showing nanoparticle morphology, (**B**) particle size distribution with a calculated average diameter of 22.99 nm, (**C**) X-ray diffraction (XRD) pattern confirming the spinel-type cubic structure, (**D**) initial magnetization curve and hysteresis loop illustrating the magnetic behavior of the nanoparticles.

Magnetic characterization of the $CoFe_2O_4$ nanoparticles is presented in Figure 4D, which includes the initial magnetization curve and the hysteresis loop. The nanoparticles exhibited a saturation magnetization (M_s) of 60 emu/g, a remanent magnetization (M_x) of 22 emu/g, a coercivity (H_c) of 1457 Oe, and an initial magnetic susceptibility (χ) of 0.009 emu/g·Oe.

The transmission electron microscopy (TEM) micrograph of the $Co_{108}Ni_{0.2}Fe_2O_4$ nanoparticles is shown in Figure 5A. A particle size count was performed, and the corresponding histogram is presented in Figure 5B. A normal distribution curve was fitted to the histogram, yielding an average particle size of 25.13 nm with a standard deviation of 6.5 nm. The X-ray diffraction pattern of the $Co_{0.8}Ni_{0.2}Fe_2O_4$ sample Figure 5C, similarly to the undoped sample, showed all diffraction peaks indexed to a cubic phase with Fd-3m structure, space group 227.

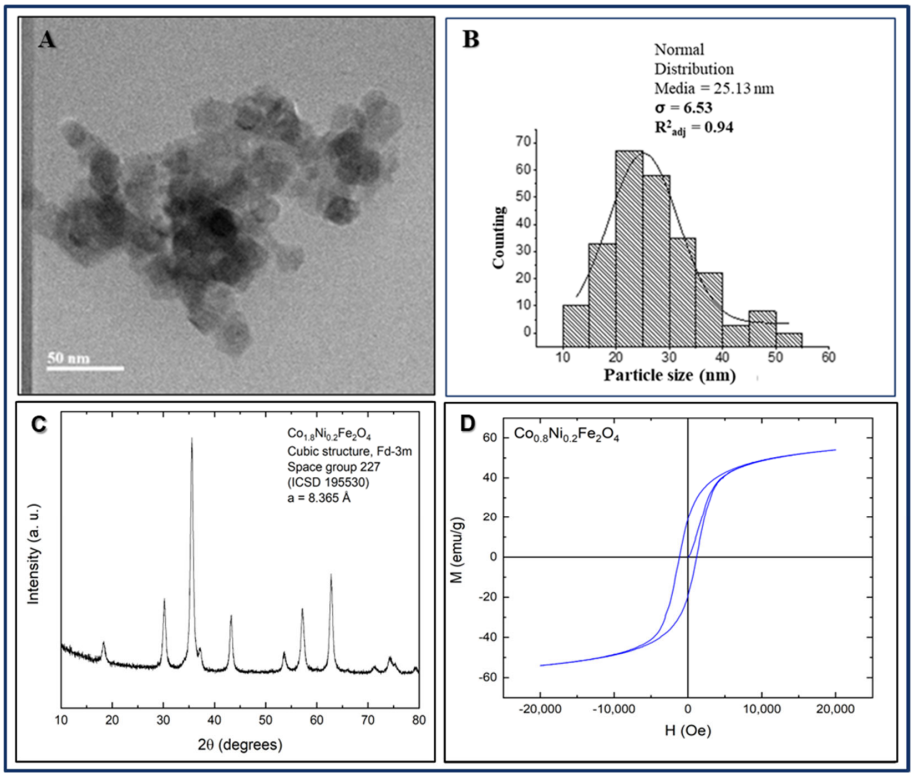


Figure 5. Characterization of $Co_{0.8}Ni_{0.2}Fe_2O_4$ nanoparticles, comprising: (**A**) TEM micrograph displaying particle morphology, (**B**) particle size distribution, with an average diameter of 25.13 nm, (**C**) XRD pattern similar to the undoped particles, (**D**) magnetic properties demonstrated through the initial magnetization curve and hysteresis loop.

The calculated lattice parameter was 8.365 Å, which is smaller than that of pure cobalt ferrite. This reduction is attributed to the difference in ionic radii between Ni^{2+} (0.69 Å) and Co^{2+} (0.745 Å). For the $Co_{0.8}Ni_{0.2}Fe_2O_4$ sample (Figure 5D), the initial magnetic susceptibility was 0.01 emu/g·Oe, the saturation magnetization was 54 emu/g, the remnant magnetization was 19 emu/g, and the coercivity was 1192 Oe.

The pure cobalt ferrite sample exhibited the highest values of *Hc*, *Mr*, and *Ms*. The decrease in saturation magnetization observed in the nickel-doped sample can be explained by the lower magnetic moment of the Ni^{2+} ion (2 μB) compared to that of the Co^{2+} ion (3 μB). The reduction in coercive field is attributed to a decrease in magnetocrystalline anisotropy due to the increased Ni content.

3.4. Antimicrobial Activity of SnO_2 Films Against C.albicans Exposed to Physical Treatments and Metallic Nanoparticles on Dry Surfaces

Control SnO_2 films exhibited increased *C.albicans* viability compared to the glass surface, with a relative growth rate of 148%. In contrast, SnO_2 films doped with metallic nanoparticles showed notable antifungal activity even without exposure to UVC or electrical current: films containing Cu_2O nanoparticles (SnO_2 + Cu_2ONP) achieved 82.5%

inhibition of fungal growth, while those doped with silver nanoparticles (SnO_2 + AgNP) reached 85.2% inhibition. When physical treatments were applied, the antimicrobial efficacy of both doped films was further enhanced, resulting in complete suppression of *C. albicans* growth, corresponding to 100% inhibition (Figure 6).

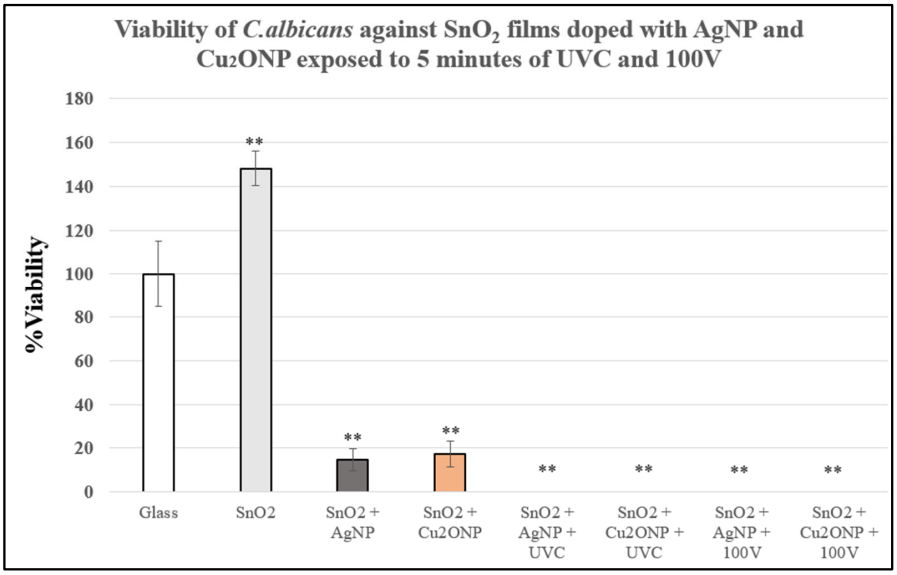


Figure 6. *C. albicans* viability assay following exposure to UVC irradiation and 100 V on SnO_2 film surfaces, with or without Cu_2O and Ag nanoparticles. Inert glass surfaces were used as negative controls. Asterisks indicate statistically significant differences ($p < 0.01$).

Exposure of *C. albicans* to UVC radiation (5 min) on a glass surface resulted in 55.7% inhibition. Under the same conditions, SnO_2 films achieved a significantly higher inhibition rate of 86.3%. When exposed solely to an electric field of 100 V, the SnO_2 films demonstrated 94.4% inhibition. To assess potential synergistic effects between UVC and electrical current, SnO_2 films were simultaneously exposed to both treatments, leading to complete inhibition (100%) of *C. albicans* growth in all experimental replicates (Figure 7).

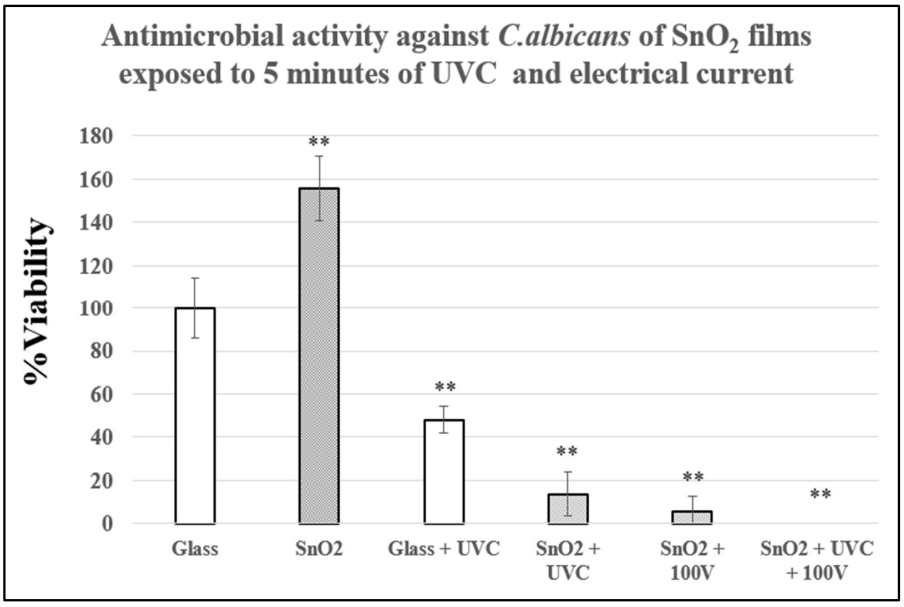


Figure 7. Antimicrobial activity against *C. albicans* following 5 min exposure to UVC irradiation and 100 V (1–2 mA) electrical current. Data represent the mean inhibition rates across replicates. Asterisks indicate statistically significant differences are indicated ($p < 0.01$).

SEM analysis showed that *C. albicans* produced biofilms in every sample that was not exposed to UVC (Figure 8A); this is more evident in SnO_2 films doped with nanoparticles (Figure 8C,D). However, when yeast cells are exposed to UVC, the biofilms are no longer synthesized (Figure 8B). Morphological changes were more evident in samples containing AgNP, since cell walls appear heavily damaged (Black arrow, Figure 8C). *C. albicans* on samples containing Cu_2ONP produced high quantities of biofilms, hindering the observation of cell morphology (Black arrow, Figure 8D).

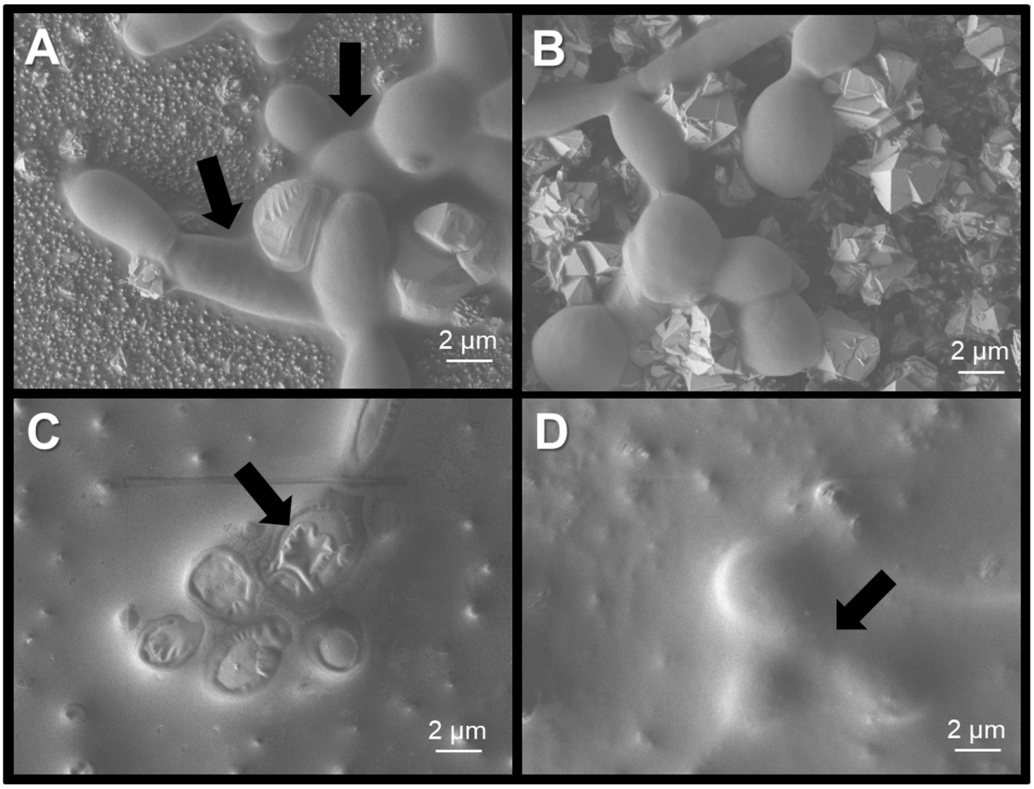


Figure 8. SEM analysis of SnO_2 films inoculated with *C. albicans*. (**A**) Presence of biofilm (indicated by black arrows) surrounding yeast cells on the surface of undoped SnO_2 films. (**B**) Biofilms are no longer visible following UVC exposure. (**C**) On SnO_2 films doped with AgNPs, damage to the cell wall is observed in most yeast cells (indicated by black arrow). (**D**) SnO_2 films doped with Cu_2O nanoparticles show extensive biofilm coverage.

3.5. Antimicrobial Assays of Ferrite Nanoparticles Exposed to Physical Treatments

Inhibition of ferrite nanoparticles in aqueous solutions was measured immediately after exposure to UVC, 100V and a magnetic field (2959 Gauss). $CoFe_2O_4$ and $Co_{0.8}Ni_{0.2}Fe_2O_4$ nanoparticles had similar performances in *C. albicans* viability assays. Cobalt ferrites inhibited 26.1% and cobalt–nickel ferrites 30.4% of *C. albicans* growth even when they were not exposed to physical treatments. When exposed to UVC or electrical current, either nanoparticle had a significant change in their antimicrobial activity compared with physical treatments without ferrite nanoparticles. Only the magnetic field was a relevant factor that had synergy with the nanoparticle toxicity (Table 1).

Table 1. Inhibition percentages of ferrite nanoparticles against *C. albicans* under physical treatments in aqueous media. $p < 0.01$ (**).

	Without ferrites	$CoFe_2O_4$	$Co_{0.8}Ni_{0.2}Fe_2O_4$
No physical treatment	0%	26.1% (*)	30.4% (**)
100V	33.88%	21.9%	27.4%
UVC	27.8%	29.5%	40.4% (**)
2959G	0%	33.1% (**)	35.8% (**)
100V + 2959G	33.8%	32.5%	26.7%
100V + UVC	38.1%	29.6%	28.9%
100V + UVC + 2959G	38.1%	30.91%	25.1%

The morphology of *C. albicans* after exposure to ferrites was studied using SEM; as a comparison point, non-treated yeasts were used (Figures 9A and 10A). Cells exposed to $CoFe_2O_4$ and $Co_{0.8}Ni_{0.2}Fe_2O_4$ nanoparticles showed nanoparticle cumulus on the surface of cell walls as observed in Figures 9B and 10B. Cell wall damage observed after exposure to UVC was similar in both treatments (Figures 9C and 10C). $CoFe_2O_4$ nanoparticles are susceptible to magnetic fields, since its accumulation was grater on the surface of *C. albicans* (Figure 9D). On the other hand, $Co_{0.8}Ni_{0.2}Fe_2O_4$ nanoparticles behavior was not altered when exposed to the same magnetic field, as can be observed on Figure 10D.

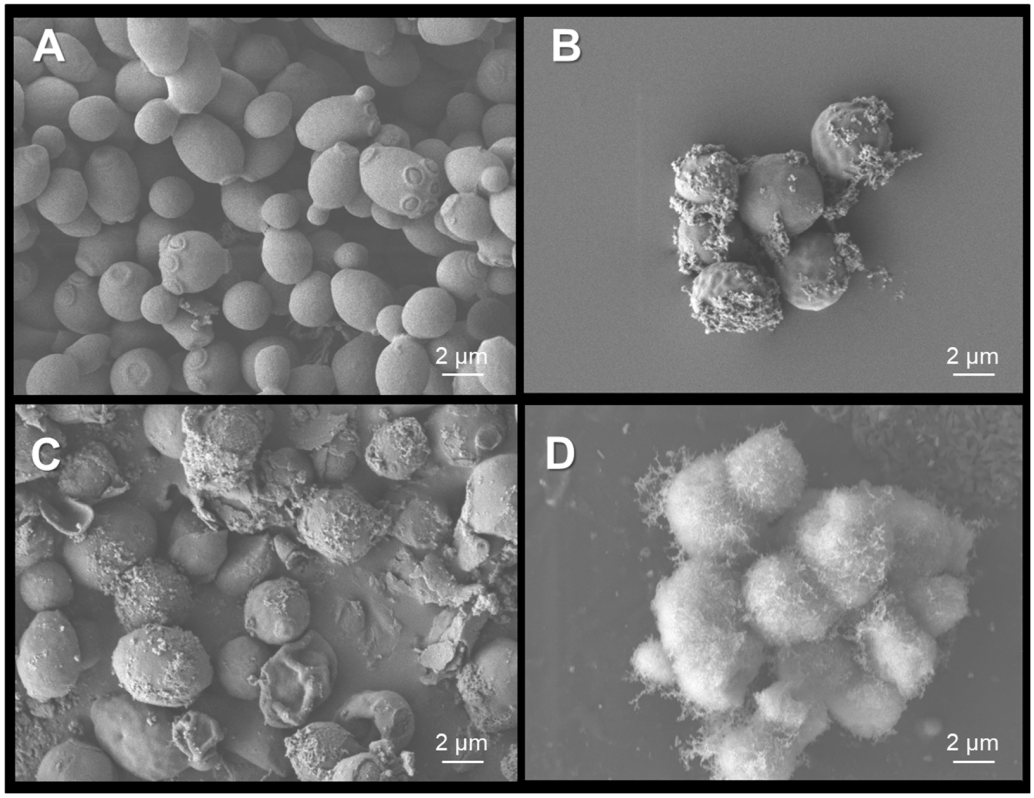


Figure 9. SEM micrographs showing morphological changes in *C. albicans*: (**A**) Control (no exposure to ferrites or treatments), (**B**) C. albicans exposed to $CoFe_2O_4$, (**C**) *C. albicans* exposed to $CoFe_2O_4$ and UVC radiation, (**D**) *C. albicans* exposed to $CoFe_2O_4$, UVC radiation, electrical current, and a magnetic field.

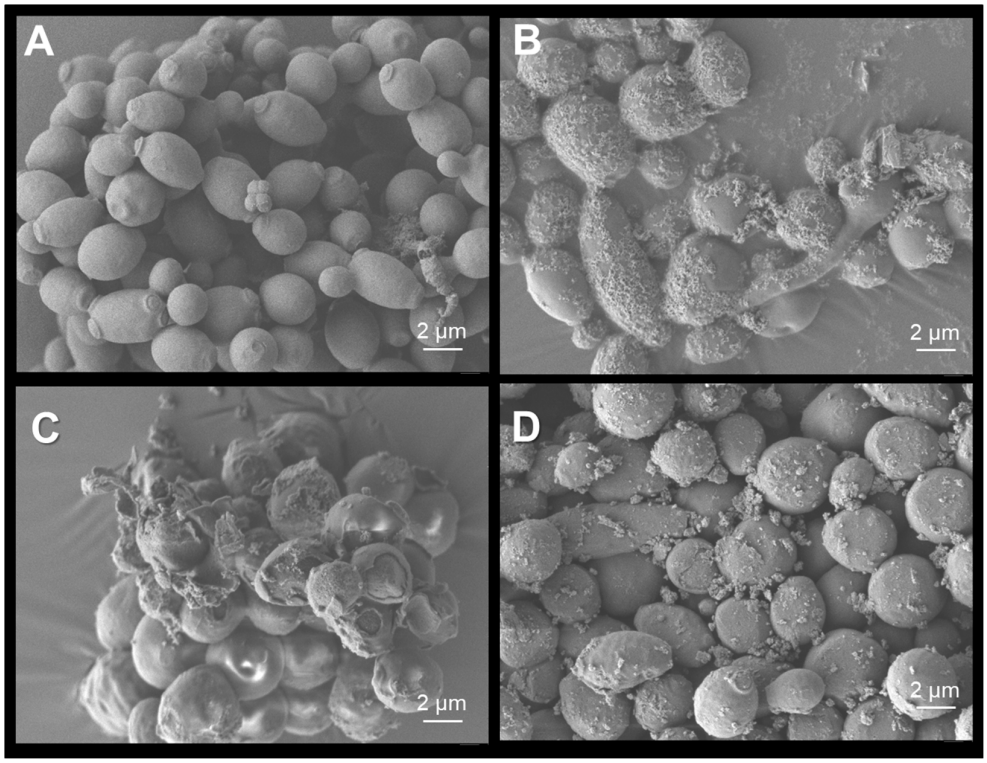


Figure 10. SEM analysis of *C. albicans* exposed to $Co_{0.8}Ni_{0.2}Fe_2O_4$ and physical treatments: (**A**) Untreated control, (**B**) exposure to cobalt–nickel ferrites, (**C**) cobalt–nickel ferrites and UVC radiation, (**D**) cobalt–nickel ferrites combined with UVC radiation, electrical current, and magnetic field.

The accumulation of $CoFe_2O_4$ and $Co_{0.8}Ni_{0.2}Fe_2O_4$ nanoparticles was confirmed using backscattered electron imaging, which allows contrast based on atomic number. This technique was used to differentiate the nanoparticles from organic matter, which can appear similar in conventional micrographs (Figure 11A). The bright (white) structures observed in Figure 11B correspond to heavier elements (indicative of the nanoparticles) while the surrounding organic cellular components appear in varying shades of gray.

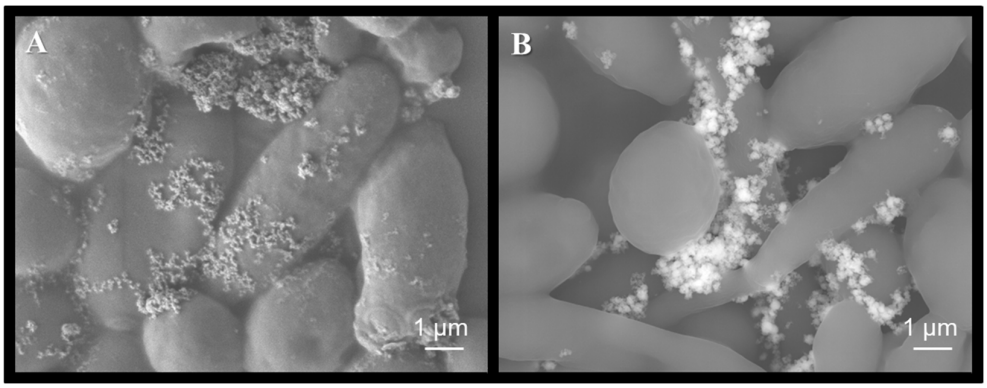


Figure 11. $CoFe_2O_4$ and $Co_{0.8}Ni_{0.2}Fe_2O_4$ nanoparticles exhibit strong adhesion to the surface of *Candida albicans* ((**A**)). This interaction is further confirmed by backscattered electron imaging in (**B**), which highlights the presence of nanoparticles on the fungal surface.

3.6. Photocatalytic Activity of WO_3 Films on Dry Surfaces

The physicochemical characterization of the WO_3 films used in this study has been previously reported [14]. These results are not included here, as the focus of the present work is on evaluating antimicrobial activity.

Antimicrobial assays against *C. albicans* yielded the following results: WO_3 films not exposed to UVC showed a 123.8% increase in growth compared to the glass control (set at 100% viability). In contrast, all other samples exhibited reduced viability relative to the control. Specifically, the glass surface exposed to UVC showed 48.6% viability; 50 nm WO_3 films, 47.6%; 100 nm WO_3 films, 28.7%; and 200 nm WO_3 films, 13.79% (Figure 12).

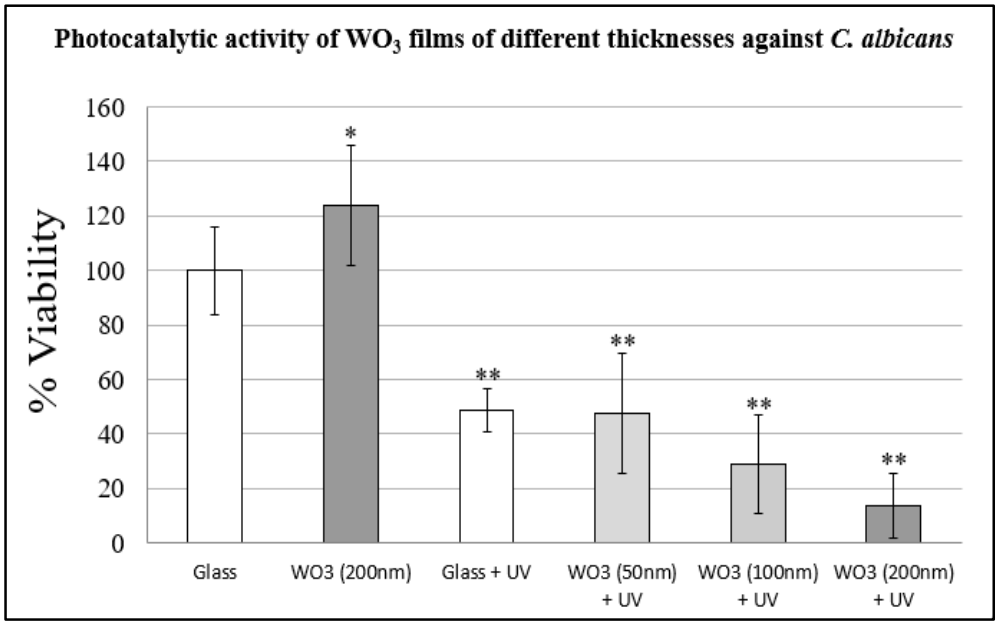


Figure 12. Viability assay of *C. albicans* exposed to UVC radiation (254 nm) for 5 min after inoculation on glass (control) and WO_3-coated surfaces. Film thickness significantly influenced fungal inhibition, with 200 nm WO_3 films demonstrating the highest efficacy. $p < 0.05$ (*), $p < 0.01$ (**).

4. Discussion

Antimicrobial tests showed that, in the absence of nanoparticles, UVC exposure, or electrical current, SnO_2 films exhibited a similar behavior than WO_3 films, resulting in increased *C. albicans* viability compared to the glass surface. This effect may be attributed to the fact that the chemical compounds in these films are not inherently antimicrobial. Instead, their composition (potentially combined with mild ROS generation under ambient light) may create a mildly stressful environment that stimulates fungal metabolism. In contrast, the glass surface acts as a chemically inert substrate. Under nutrient-rich conditions, this metabolic stimulation may accelerate the fungal life cycle, leading to a higher number of colony-forming units (CFUs) than on glass control. This phenomenon warrants further investigation to assess potential changes in the expression of genes involved in the cellular cycle. This hypothesis is supported by previous studies that suggest that *C. albicans* possess a very adaptable metabolism that changes based on hypoxia, nutrient availability or the presence of antimicrobial compounds [19–21].

The SnO_2 films doped with Cu_2ONPs and AgNPs exhibited a high inhibition rate even in the absence of UVC irradiation or electrical stimulation. This behavior was expected given the well-documented antimicrobial properties of both silver and copper nanoparticles [22–25]. The film's strong antimicrobial activity under dry conditions is particularly notable, especially considering that only a small number of nanoparticles (approximately 1% of the film's total mass) were deposited on their surfaces. Given an average film surface area of 1 cm^2, the estimated nanoparticle mass per film ranged from 5 to 10 μg.

SEM analysis in Figure 8 shows the damage on cell walls of *C. albicans* on SnO_2 films doped with AgNP, cell wall rupture is consistent with previous work in which this microorganism was exposed to AgNP in aqueous media [26]. This finding aligns with

previous studies demonstrating the efficacy of surface-applied nanoparticles in antimicrobial coatings [27,28]. Although Cu_2O nanoparticles exhibited a high inhibition rate, no morphological changes were observed in the SEM micrographs. This observation is consistent with previous reports indicating that the toxicity of Cu^+/Cu^{2+} ions is primarily associated with DNA damage and metabolic disruption, rather than structural damage to the cell wall [29].

The photocatalytic activity of SnO_2 films as disinfectant and pollutant degradation is also well documented [5,30,31], and the potential inhibition activity is improved by the presence of metallic nanoparticles due to their ability of absorbing photons more efficiently and transferring the energy to the semiconductor material, resulting in a more efficient process [32,33]. The microscopic analysis of Figure 8 showed that *C. albicans* no longer produces biofilms after exposure to UVC on SnO_2 films, which is consistent with previous reports [34], this could be a consequence of a change in the expression of regulatory genes, due to direct DNA damage or methylation [35] caused by UVC radiation. As mentioned before, nanoparticles alone do not inhibit biofilm synthesis, and the use of UVC as an additional disinfection measure should be considered in doped SnO_2 films to guarantee a high-level surface disinfection.

The use of electrical current for disinfecting semiconductor surfaces is uncommon and has been scarcely reported in the literature. However, this method has been successfully applied in the elimination of pathogenic microorganisms from air [36] and water [37], and on the surfaces of various devices [38]. In this study, SnO_2 films were synthesized with a thickness of 1 μm to ensure sufficient electrical conductivity, as thinner films proved unsuitable for current-based disinfection assays. The voltage was set at 100 V in order to achieve a rapid disinfection, but also, this voltage poses no significant risk to human safety. The current was maintained between 1 and 2 mA. It is crucial to keep the amperage low, as the inherent resistance of semiconductor materials can generate heat, potentially damaging the thin films deposited on glass substrates; additionally, limiting the current minimizes the risk of injury to the operator. After exposure to the electrical field, most samples achieved 100% inhibition of *C. albicans* growth; however, in some replicates, inhibition reached only 95%, this influenced the viability bars shown in Figure 7. The hypothesis is that slight differences in film conductivity across samples caused the inability of some films to completely inhibit the microorganism; however, electrical disinfection of dry semiconductor surfaces was highly successful. Films doped with nanoparticles and exposed to UVC and electrical current were analyzed by SEM; however, those micrographs were not included in this work, since they were completely free of *C. albicans* cells.

The synergistic effect between UVC radiation and electrical current was anticipated, as similar combinations have been reported in solar energy applications for the degradation of water pollutants and renewable energy generation [39,40] and as antimicrobial treatment in aqueous media against *C. albicans* [41]. This outcome was further supported by the fact that both treatments individually achieved high inhibition rates, as shown in Figure 7. When both UVC and electrical current were applied simultaneously on a dry photocatalytic SnO_2 surface, all samples exhibited 100% inhibition, with no colony-forming units (CFUs) observed under the optical microscope. Nanoparticles and applied electrical fields can enhance the efficiency of photocatalytic semiconductors. The antimicrobial synergy observed experimentally can be attributed to the influence of free electrons and/or dopants, which induce changes in the Fermi energy level, promote band bending, and improve the separation of electron-hole (e^-/h^+) pairs. These effects collectively lead to more efficient photocatalysis, particularly by facilitating the conversion of oxygen molecules into reactive oxygen species (ROS), which are responsible for microbial inactivation [42]. This observed

synergy highlights the strong potential of this combined approach for the development of more effective disinfection strategies in hospital environments.

The inhibition activity of $CoFe_2O_4$ and $Co_{0.8}Ni_{0.2}Fe_2O_4$ nanoparticles was in the range of 21.9% to 40.4% (Table 1); however, the assays were performed in aqueous media that contained components from the Dextrose Sabouraud broth, the combination of those factors could reduce the effectiveness of UVC [43] and electrical current treatments [44]. $CoFe_2O_4$ nanoparticles had an improvement in their antimicrobial activity in the presence of a magnetic field, increasing the percentage of inhibition from 26.1% (without magnetic field) to 36.1%. On the other hand, $Co_{0.8}Ni_{0.2}Fe_2O_4$ nanoparticles had a similar improvement in the presence of UVC, increasing from 30.4% (without UVC) to 40.4%. The presence of Nickel changed the affinity of the ferrites to magnetic fields and UVC radiation, but their inhibition rates were very similar overall.

An outcome that could be of potential biomedical use is the fact that both kind of ferrites had a high affinity for the cellular wall of *C. albicans*, as shown in Figures 9–11. This could be explained by the fact that the cell wall has a predominant presence of positively charged amino acids [5]; the magnetic field had an strong influence in $CoFe_2O_4$ nanoparticles, as can be observed in Figure 9D, their affinity for Candida's cell wall was increased notably. Even though the inhibition rates were not higher than other treatments, the tendency of the ferrites to adhere to yeast cells is a characteristic that could be useful in the design of drug carriers of low toxicity and sensitive to magnetic fields.

The antimicrobial activity of WO_3 thin films is associated with the generation of reactive oxygen species (ROS) and hydrogen peroxide (H_2O_2), as well as the material's ability to interact with UVC radiation to induce electron transfer processes [45]. This activity is enhanced in thicker films due to increased photon absorption, which leads to greater photocatalytic efficiency [46]. The results obtained in the present study support these findings, demonstrating that film thickness significantly influences antimicrobial performance. Under 5 min of UVC exposure, the thinnest film (50 nm) showed no significant difference in *C. albicans* growth inhibition compared to the glass control (52.4% and 51.3%, respectively). In contrast, 100 nm films achieved 71% inhibition, while 200 nm films reached 86.2% inhibition. The SEM analysis performed on WO_3 films inoculated with *C. albicans* did not show any significant changes in morphology or structural damage, and results were similar to those observed on SnO_2 + Cu_2ONP films. Photocatalytic films were highly successful in the rapid photocatalytic disinfection and are promising coatings applicable on surfaces of the hospital environment or medical devices; however, more studies are necessary to evaluate their efficiency against other important nosocomial microorganisms.

5. Conclusions

Based on the obtained results, WO_3 and SnO_2 photocatalytic films are effective materials for UVC-assisted disinfection processes. These surfaces enable significantly faster microbial inactivation due to their ability to enhance the effects of high-energy photons and generate reactive oxygen species (ROS) from oxygen and water molecules. The antimicrobial performance of these films can be further enhanced through the incorporation of metallic nanoparticles and the application of low-voltage electrical current. These combined treatments produce a synergistic effect that results in high levels of disinfection or complete sterilization of dry surfaces, highlighting their strong potential for applications in hospital and clinical environments.

$CoFe_2O_4$ and $Co_{0.8}Ni_{0.2}Fe_2O_4$ nanoparticles also represent a promising antimicrobial magnetic and photocatalytic material, further enhancing their efficiency in the presence of magnetic and electric fields. Moreover, the propensity of these particles to adhere to the

cell walls of *C. albicans* could be leveraged for the design of future antimicrobial treatments as safe drug carrier nanoparticles.

Author Contributions: Conceptualization, C.A.-Q. and M.C.G.-C.; data curation, M.C.G.-C.; formal analysis, C.A.-Q., J.C.C. and M.C.G.-C.; funding acquisition, C.A.-Q., A.R.C.-G., C.M.Q.-F., M.A.F.-P. and M.C.G.-C.; investigation, C.A.-Q., R.J.S.-H., A.A.C.-M., F.A.H.-O., F.E.D.-C., C.L.-P. and I.R.A.-G.; methodology, C.A.-Q., R.J.S.-H., A.A.C.-M., F.A.H.-O., F.E.D.-C. and A.R.C.-G.; project administration, C.A.-Q. and M.C.G.-C.; resources, C.A.-Q., A.R.C.-G., C.M.Q.-F. and M.A.F.-P.; software, J.C.C.; supervision, C.A.-Q., M.C.G.-C., R.J.S.-H., C.L.-P., A.R.C.-G., C.M.Q.-F. and M.A.F.-P.; validation, R.J.S.-H. and C.L.-P.; visualization, C.A.-Q.; original draft, C.A.-Q., R.J.S.-H. and M.C.G.-C.; writing—review and editing, C.A.-Q. and M.C.G.-C. All authors have read and agreed to the published version of the manuscript.

Funding: This research received no external funding.

Institutional Review Board Statement: Not applicable.

Informed Consent Statement: Not applicable.

Data Availability Statement: All data supporting the findings of this study are available within the article.

Acknowledgments: We would like to thank the support of the Autonomous University of Chihuahua (UACH) and the Center of Investigation in Advanced Materials of Chihuahua (CIMAV) on the realization of this research work.

Conflicts of Interest: The authors declare no conflict of interest.

References

1. Warris, A.; Pana, Z.-D.; Oletto, A.; Lundin, R.; Castagnola, E.; Lehrnbecher, T.; Groll, A.H.; Roilides, E. Etiology and Outcome of Candidemia in Neonates and Children in Europe: An 11-year Multinational Retrospective Study. *Pediatr. Infect. Dis. J.* **2020**, *39*, 114–120. [CrossRef]
2. Özenen, G.G.; Bal, Z.S.; Avcu, G.; Yazici, P.O.; Karakoyun, M.; Metin, D.Y.; Polat, S.H. Evaluation of candidemia in children at a university hospital: A retrospective cohort. *Mycoses* **2023**, *66*, 367–377. [CrossRef] [PubMed]
3. Román-Aguirre, M.; Barraza-Jimenez, D.; Leyva-Porras, C.; Peinado-Villalobos, R.; Molina-Jáquez, D.; Olivas-Espino, J.A.; Castillo-González, A.R.; Camarillo-Cisneros, J.; Favila-Pérez, M.A.; Quiñonez-Flores, C.M.; et al. Mechanisms of Integration and Release of $AgNO_3$ in Chitosan Films and Their Interaction with Nosocomial Pathogens. *Coatings* **2024**, *14*, 1453. [CrossRef]
4. Jeck, J.; Jakobs, F.; Kurte, M.S.; Cornely, O.A.; Kron, F. Health-economic modelling of cost savings due to the use of rezafungin based on a German cost-of-illness study of candidiasis. *JAC Antimicrob. Resist.* **2023**, *5*, dlad079. [CrossRef] [PubMed]
5. Faudoa-Arzate, A.; Camarillo-Cisneros, J.; Castillo-González, A.R.; Favila-Pérez, M.A.; Sáenz-Hernández, R.J.; Realyvazquez-Guevara, P.R.; Arzate-Quintana, C. Disinfection mechanism of the photocatalytic activity of SnO_2 thin films against *Candida albicans*, proposed from experimental and simulated perspectives. *Can. J. Microbiol.* **2021**, *67*, 667–676. [CrossRef]
6. Micelly-Moreno, J.; Barreto-Santamaría, A.; Arévalo-Pinzón, G.; Firacative, C.; Gómez, B.L.; Escandón, P.; Patarroyo, M.A.; Muñoz, J.E. Therapeutic Use of the Antimicrobial Peptide PNR20 to Resolve Disseminated Candidiasis in a Murine Model. *J. Fungi* **2023**, *9*, 1149. [CrossRef]
7. Jothi, R.; Hong, S.T.; Enkhtsatsral, M.; Pandian, S.K.; Gowrishankar, S. ROS mediated anticandidal efficacy of 3-Bromopyruvate prevents vulvovaginal candidiasis in mice model. *PLoS ONE* **2023**, *18*, e0295922. [CrossRef]
8. Widodo, T.T.; Siswomiharjo, W.; Sunarintyas, S.; Yulianto, D.K. Effect of method and concentration of titanium dioxide addition on anti-biofilm ability in extraoral maxillofacial prosthetic fungus. *Int. J. Adv. Med.* **2022**, *10*, 1–9. [CrossRef]
9. Binns, R.; Li, W.; Wu, C.D.; Campbell, S.; Knoernschild, K.; Yang, B. Effect of Ultraviolet Radiation on *Candida albicans* Biofilm on Poly(methylmethacrylate) Resin. *J. Prosthodont.* **2020**, *29*, 686–692. [CrossRef]
10. Ghosh, S.; Mukherjee, R.; Basak, D.; Haldar, J. One-Step Curable, Covalently Immobilized Coating for Clinically Relevant Surfaces That Can Kill Bacteria, Fungi, and Influenza Virus. *ACS Appl. Mater. Interfaces* **2020**, *12*, 27853–27865. [CrossRef]
11. Dumpati, S.; Naroo, S.A.; Shah, S.; Dutta, D. Antimicrobial Efficacy of an Ultraviolet-C Device against Microorganisms Related to Contact Lens Adverse Events. *Antibiotics* **2022**, *11*, 699. [CrossRef] [PubMed]
12. Politano, G.G. Optical Properties of Thick TiO_2-P25 Films. *Nanomaterials* **2025**, *15*, 99. [CrossRef] [PubMed]

13. Sukriti, C.P. Effect of pH Values on the Structural, Optical and Electrical Properties of SnO_2 Nanostructures. *Optik* **2019**, *181*, 768–778. [CrossRef]
14. Kim, S.; Chang, H.-K.; Kim, K.B.; Kim, H.-J.; Lee, H.-N.; Park, T.J.; Park, Y.M. Highly Porous SnO_2/TiO_2 Heterojunction Thin-Film Photocatalyst Using Gas-Flow Thermal Evaporation and Atomic Layer Deposition. *Catalysts* **2021**, *11*, 1144. [CrossRef]
15. Kuang, Y.; Zardetto, V.; van Gils, R.; Karwal, S.; Koushik, D.; Verheijen, M.A.; Black, L.E.; Weijtens, C.; Veenstra, S.; Andriessen, R.; et al. Low-Temperature Plasma-Assisted Atomic-Layer-Deposited SnO_2 as an Electron Transport Layer in Planar Perovskite Solar Cells. *ACS Appl. Mater. Interfaces* **2018**, *10*, 30367–30378. [CrossRef]
16. Akyildiz, H.I.; Diler, S.; Islam, S. Evaluation of TiO_2 and ZnO atomic layer deposition coated polyamide 66 fabrics for photocatalytic activity and antibacterial applications. *J. Vac. Sci. Technol* **2021**, *39*, 022405. [CrossRef]
17. Mwathe, P.; Musembi, R.; Munji, M.; Odari, V.; Munguti, L.; Ntilakigwa, A.; Nguu, J.; Muthoka, B. Effect of Surface Passivation on Electrical Properties of Pd-F:SnO_2 Thin Films Prepared by Spray Pyrolysis Technique. *Coatings* **2014**, *4*, 747–755. [CrossRef]
18. Sáenz-Hernández, R.J.; Herrera-Pérez, G.M.; Uribe-Chavira, J.S.; Grijalva-Castillo, M.C.; Elizalde-Galindo, J.T.; Matutes-Aquino, J.A. Correlation between Thickness and Optical Properties in Nanocrystalline γ-Monoclinic WO_3 Thin Films. *Coatings* **2022**, *12*, 1727. [CrossRef]
19. Burgain, A.; Tebbji, F.; Khemiri, I.; Sellam, A. Metabolic Reprogramming in the Opportunistic Yeast *Candida albicans* in Response to Hypoxia. *mSphere* **2020**, *5*, e00913–e00919. [CrossRef]
20. Dunker, C.; Polke, M.; Schulze-Richter, B.; Schubert, K.; Rudolphi, S.; Gressler, A.E.; Pawlik, T.; Prada-Salcedo, J.P.; Niemiec, M.J.; Slesiona-Künzel, S.; et al. Rapid proliferation due to better metabolic adaptation results in full virulence of a filament deficient *Candida albicans* strain. *Nat. Commun.* **2021**, *12*, 3899. [CrossRef]
21. Liboro, K.; Yu, S.R.; Lim, J.; So, Y.S.; Bahn, Y.S.; Eoh, H.; Park, H. Transcriptomic and Metabolomic Analysis Revealed Roles of Yck2 in Carbon Metabolism and Morphogenesis of *Candida albicans*. *Front. Cell. Infect. Microbiol.* **2021**, *11*, 636834. [CrossRef] [PubMed]
22. Gheni, M.R.; Odaa, N.H. The antimicrobial activity of melanin-mediated synthesis of silver nanoparticles. *Egypt. J. Hosp. Med.* **2023**, *90*, 3383–3394. [CrossRef]
23. Nam, S.; Easson, M.W.; Jordan, J.H.; He, Z.; Zhang, H.; Cintrón, M.S.; Chang, S. Unveiling the hidden value of cotton gin waste: Natural synthesis and hosting of silver nanoparticles. *ACS Omega* **2023**, *8*, 31281–31292. [CrossRef] [PubMed]
24. SadrHaghighi, A.; Sarvari, R.; Fakhri, E.; Poortahmasebi, V.; Sedighnia, N.; Torabi, M.; Mohammadzadeh, M.; Azhiri, A.H.; Eskandarinezhad, M.; Moharamzadeh, K.; et al. Copper-nanoparticle-coated melt-blown facemask filter with antibacterial and sars-cov-2 antiviral ability. *ACS Appl. Nano Mater.* **2023**, *6*, 12849–12861. [CrossRef]
25. Raja, F.N.S.; Worthington, T.; Martin, R.A. The antimicrobial efficacy of copper, cobalt, zinc and silver nanoparticles: Alone and in combination. *Biomed. Mater.* **2023**, *18*, 045003. [CrossRef]
26. Arzate-Quintana, C.; Sánchez-Ramírez, B.; Infante-Ramírez, R.; Piñón-Castillo, H.A.; Montes-Fonseca, S.L.; Duarte-Moller, A.; Luna-Velasco, A.; Solís-Martínez, F.J.; Orrantia-Borunda, E. Toxicity effects in pathogen microorganisms exposed to silver nanoparticles. *Nanosci. Nanotechnol. Lett.* **2017**, *9*, 165–173. [CrossRef]
27. Rezić, I.; Škoc, M.S.; Majdak, M.; Jurić, S.; Stracenski, K.S.; Vinceković, M. Functionalization of polymer surface with antimicrobial microcapsules. *Polymers* **2022**, *14*, 1961. [CrossRef]
28. Burdușel, A.; Gherasim, O.; Grumezescu, A.M.; Mogoantă, L.; Ficai, A.; Andronescu, E. Biomedical applications of silver nanoparticles: An up-to-date overview. *Nanomaterials* **2018**, *8*, 681. [CrossRef]
29. Santoro, A.M.; Monaco, I.; Attanasio, F.; Lanza, V.; Pappalardo, G.; Tomasello, M.F.; Cunsolo, A.; Rizzarelli, E.; De Luigi, A.; Salmona, M.; et al. Copper(II) ions affect the gating dynamics of the 20S proteasome: A molecular and in cell study. *Sci Rep.* **2016**, *16*, 33444. [CrossRef]
30. Aihemaiti, X.; Wang, X.; Li, Y.; Wang, Y.; Xiao, L.; Ma, Y.; Qi, K.; Zhang, Y.; Liu, J.; Li, J. Enhanced photocatalytic and antibacterial activities of S-scheme SnO_2/Red phosphorus photocatalyst under visible light. *Chemosphere* **2022**, *296*, 134013. [CrossRef]
31. Priyadharsan, A.; Palanisamy, G.; Pragasan-L, A.; Albeshr, M.F.; Alrefaei, A.F.; Lee, J.; Liu, X. Photocatalytic degradation of organic pollutants and inactivation of pathogens under visible light via SnO_2/rGO composites. *Chemosphere* **2023**, *335*, 139102.
32. Fang, M.; Tan, X.; Liu, Z.; Hu, B.; Wang, X. Recent Progress on Metal-Enhanced Photocatalysis: A Review on the Mechanism. *Research* **2021**, *2021*, 9794329. [CrossRef] [PubMed]
33. Długosz, O.; Banach, M. Continuous synthesis of photocatalytic nanoparticles of pure ZnO and ZnO modified with metal nanoparticles. *J. Nanostruct. Chem.* **2021**, *11*, 601–617. [CrossRef]
34. Arzate-Quintana, C.; Leyva-Porras, C.; Favila-Pérez, M.A.; Castillo-González, A.R.; Quiñonez-Flores, C.M.; Faudoa-Arzate, A. Biofilm integrity and cytomorphology of *Candida albicans* after exposure to UV-light on ZnO thin films: SEM Analysis. *Microsc. Microanal.* **2021**, *27* (Suppl. 1), 1896–1898. [CrossRef]
35. Gryzińska, M.; Kot, B.; Dudzińska, E.; Biernasiuk, A.; Jakubczak, A.; Malm, A.; Andraszek, K. Changes in the level of DNA methylation in *Candida albicans* under the influence of physical and chemical factors. *Int. J. Mol. Sci.* **2023**, *24*, 15873. [CrossRef]

36. Huo, Z.Y.; Kim, Y.J.; Suh, I.Y.; Lee, D.M.; Lee, J.H.; Du, Y.; Wang, S.; Yoon, H.J.; Kim, S.W. Triboelectrification induced self-powered microbial disinfection using nanowire-enhanced localized electric field. *Nat. Commun.* **2021**, *12*, 3693. [CrossRef]
37. Zhou, J.; Wang, T.; Yu, C.; Xie, X. Locally enhanced electric field treatment (LEEFT) for water disinfection. *Front. Environ. Sci. Eng.* **2020**, *14*, 78. [CrossRef]
38. Freebairn, D.; Linton, D.; Harkin-Jones, E.; Jones, D.S.; Gilmore, B.F.; Gorman, S.P. Electrical methods of controlling bacterial adhesion and biofilm on device surfaces. *Expert. Rev. Med. Devices* **2013**, *10*, 85–103. [CrossRef]
39. Miao, W.; He, W.; Fang, Z.; Guo, K.; Yang, Z. Internal electric field enhanced photocatalytic transfer hydrogenation in heterojunction: Modulations and applications. *Mater. Today Energy* **2023**, *37*, 101408. [CrossRef]
40. Dai, B.; Guo, J.; Gao, C.; Yin, H.; Xie, Y.; Lin, Z. Recent Advances in Efficient Photocatalysis via Modulation of Electric and Magnetic Fields and Reactive Phase Control. *Adv. Mater.* **2023**, *35*, 2210914. [CrossRef]
41. Ruelas-Casas, V.J.; Ramírez-Valdespino, C.A.; Quiñonez-Flores, C.M.; Castillo-González, A.R.; Ramos-Moctezuma, I.R.; González-Chávez, S.A.; Caballero-Hernández, D.E.; Arzate-Quintana, C. Morphology of *Candida albicans* Exposed to Electric Current Treatments and UV Radiation in Sabouraud Broth Analyzed with Scanning Electron Microscopy. *Microsc. Microanal.* **2024**, *30*, 822–823. [CrossRef]
42. Ponja, S.D.; Williamson, B.A.D.; Sathasivam, S.; Scanlon, D.O.; Parkin, I.P.; Carmalt, C.J. Enhanced electrical properties of antimony doped tin oxide thin films deposited via aerosol assisted chemical vapour deposition. *J. Mater. Chem. C* **2018**, *6*, 7257–7266. [CrossRef]
43. Melo-Solarte, D.S.; Betancur-Pérez, J.F.; Narváez-Solarte, W. Evaluación de la luz ultravioleta (UVA, UVB y UVC) como agente bactericida contra *Escherichia coli* (Migula) Castellani y Chalmers-ATCC®-25922. *Boletín Científico Cent. Mus. Mus. Hist. Nat.* **2023**, *27*, 117–126. [CrossRef]
44. Gu, J.; Liu, S.; Ni, W.; Ren, W.; Haussener, S.; Hu, X. Modulating electric field distribution by alkali cations for CO_2 electroreduction in strongly acidic medium. *Nat. Catal.* **2022**, *5*, 268–276. [CrossRef]
45. Li, H.; Lin, C.; Yang, Y.; Dong, C.; Min, Y.; Shi, X.; Wang, L.; Lu, S.; Zhang, K. Boosting Reactive Oxygen Species Generation Using Inter-Facet Edge Rich WO_3 Arrays for Photoelectrochemical Conversion. *Angew. Chem.* **2022**, *135*, e202210804.
46. Grigioni, I.; Dozzi, M.V.; Selli, E. Photoinduced electron transfer in $WO_3/BiVO_4$ heterojunction photoanodes: Effects of the WO_3 layer thickness. *J. Phys. Condens. Matter* **2019**, *32*, 014001. [CrossRef]

Disclaimer/Publisher's Note: The statements, opinions and data contained in all publications are solely those of the individual author(s) and contributor(s) and not of MDPI and/or the editor(s). MDPI and/or the editor(s) disclaim responsibility for any injury to people or property resulting from any ideas, methods, instructions or products referred to in the content.